



Article

Amorphous Sb_2S_3 Nanospheres In-Situ Grown on Carbon Nanotubes: Anodes for NIBs and KIBs

Meng Li, Fengbin Huang, Jin Pan, Luoyang Li, Yifan Zhang, Qingrong Yao, Huaiying Zhou and Jianqiu Deng *

School of Materials Science and Engineering & Guangxi Key Laboratory of Information Materials, Guilin University of Electronic Technology, Guilin 541004, China; muzi_lemon@163.com (M.L.); huang2664110462@163.com (F.H.); shengbin3@163.com (J.P.); lly15677300606@163.com (L.L.); 18174198852@163.com (Y.Z.); qingry96@guet.edu.cn (Q.Y.); zhy@guet.edu.cn (H.Z.)

* Correspondence: jqdeng@guet.edu.cn

Received: 22 August 2019; Accepted: 9 September 2019; Published: 15 September 2019



Abstract: Antimony sulfide (Sb_2S_3) with a high theoretical capacity is considered as a promising candidate for Na-ion batteries (NIBs) and K-ion batteries (KIBs). However, its poor electrochemical activity and structural stability are the main issues to be solved. Herein, amorphous Sb_2S_3 nanospheres/carbon nanotube ($\text{Sb}_2\text{S}_3/\text{CNT}$) nanocomposites are successfully synthesized via one step self-assembly method. In-situ growth of amorphous Sb_2S_3 nanospheres on the CNTs is confirmed by X-ray diffraction, field-emission scanning electron microscopy, and transmission electron microscopy. The amorphous $\text{Sb}_2\text{S}_3/\text{CNT}$ nanocomposites as an anode for NIBs exhibit excellent electrochemical performance, delivering a high charge capacity of 870 mA h g^{-1} at 100 mA g^{-1} , with an initial coulomb efficiency of 77.8%. Even at 3000 mA g^{-1} , a charge capacity of 474 mA h g^{-1} can be achieved. As an anode for KIBs, the amorphous $\text{Sb}_2\text{S}_3/\text{CNT}$ nanocomposites also demonstrate a high charge capacity of 451 mA h g^{-1} at 25 mA g^{-1} . The remarkable performance of the amorphous $\text{Sb}_2\text{S}_3/\text{CNT}$ nanocomposites is attributed to the synergic effects of the amorphous Sb_2S_3 nanospheres and 3D porous conductive network constructed by the CNTs.

Keywords: Amorphous $\text{Sb}_2\text{S}_3/\text{CNT}$ nanocomposites; High capacity; Anode; Na-ion batteries; K-ion batteries

1. Introduction

Recently, Na-ion batteries (NIBs) and K-ion batteries (KIBs) are being developed hotly as potential substitutes for Li-ion batteries (LIBs) in large-scale energy storage system, due to their natural abundance and low cost [1,2]. Owing to the large radius of Na ions (1.02 \AA) and K ions (1.38 \AA), however, it is difficult to find appropriate electrode materials, as they would need high capacities, rapid diffusion kinetics and long life cycles [3,4]. Judging from the present development of NIBs and KIBs, the research focused on cathode materials is more productive and extensive, such as layered transition metal oxides [5,6], polyanionic type compounds [7,8] and Prussian blue analogs [9,10]. For the anode materials, the available choices are limited, including the carbonaceous materials [11,12], alloys/metals [13,14], metal sulfides [15,16] and phosphides [17,18]. Among these materials, Sb_2S_3 is considered as a promising anode material for NIBs and KIBs because of its high theoretical specific capacity, and proper sodium/potassium inserting potential based on the conversion reaction and alloying reaction [19–21]. However, the insertion/extraction process of Na/K-ion in Sb_2S_3 is accompanied with large volume change and structure destruction, along with its lower conductivity, leading to the poor rate capability and cycling performance [20,22,23].

To address these problems, combining nanostructured Sb_2S_3 with carbon materials is regarded as an effective strategy [24,25]. For example, Zhao and Manthiram have reported that an amorphous

Sb₂S₃-graphite electrode for NIBs delivers a high rate capacity, a high initial coulombic efficiency and stable cycling performance, owing to the amorphous structure of Sb₂S₃ and the conductive graphite matrix [26]. Nanostructured Sb₂S₃/sulfur-doped graphene (Sb₂S₃/SGS) anodes for NIBs demonstrate a stable capacity retention of 83% for 900 cycles, with high capacities of 2 A g⁻¹ and excellent rate performances [27]. A remarkable progress on the exploration of Sb₂S₃-based anodes for NIBs has been made in the past decade. To our knowledge, however, only a few studies have been reported on the Sb₂S₃-based anodes for KIBs, including Sb₂S₃@polypyrrole (Sb₂S₃@PPy) coaxial nanorods [21], Sb₂S₃ nanoparticles (~20 nm) uniformly dispersed into a porous S,N-codoped graphene framework (Sb₂S₃-SNG) composite [23], and a multi-layered Sb₂S₃/carbon sheet (SBS/C) composite [24]. Many studies are needed to develop Sb₂S₃-based electrodes for KIBs with high capacities, enhanced rate capabilities and cycling performances. Herein, we demonstrate the feasibility of amorphous Sb₂S₃ nanospheres/carbon nanotube (Sb₂S₃/CNT) nanocomposites as anode materials for NIBs and KIBs. Electrochemical measurements indicate the high reversible capacities and superior rate performance of Sb₂S₃/CNT nanocomposites, owing to the fact that the 3D porous nanostructure of the composites can accommodate the large volume change and enhance the ionic diffusion kinetics in Sb₂S₃.

2. Materials and Methods

2.1. Materials Synthesis

The amorphous Sb₂S₃/CNT nanocomposites were simply synthesized by a one-step self-assembly method reported by Yang's group with minor modifications [28]. Firstly, 0.34 g SbCl₃ (99.9%, Alfa Aesar Chemicals Co., Ltd., Shanghai, CN) was dissolved in 30 mL ethylene glycol (EG, 99%, Merck Life Science (Shanghai) Co., Ltd. Shanghai, CN) in a capped glass bottle with magnetic stirring. Secondly, 80 mg CNTs were added in the solution when it turned colorless and was stirred for 3 min to form a black suspension. The CNTs were purchased from XFNANO Company (Nanjing, China). 0.23 g of thioacetamide (TAA, 99%, Merck Life Science (Shanghai) Co., Ltd. Shanghai, China) was then added to the suspension without stirring, and the glass bottle was sealed by tightening the cap. After standing for 24 h at room temperature, red brown powders were formed, and finally, the products were obtained by centrifugation, washing several times with deionized water and ethanol, and drying in a vacuum oven at 90 °C for 24 h. Amorphous Sb₂S₃ nanospheres were also prepared by the same procedure without the CNTs.

2.2. Materials Characterization

Powder X-ray diffraction (XRD) measurements were performed on PIXcel^{3D} X-ray diffractometer using Cu K_α radiation source to identify the crystal structure of the materials. The morphology of the products was analyzed by field emission scanning electron microscopy (FESEM, Hitachi SU-70, Hitachi High-Technologies Corporation, Tokyo, Japan). Transmission electron microscopy (TEM) and high-resolution TEM (HRTEM) images were recorded by using a transmission electron microscope (Tecnai G2 F20, FEI Company, Hillsboro, Oregon, USA). The content of the CNTs was evaluated by an acid dissolution method. Typically, 3.0 g nanocomposites were dissolved in 50 mL concentrated hydrochloric acid (6 M). The CNTs were collected by centrifugation and washed several times with deionized water and ethanol, and then dried in a vacuum oven at 90 °C for 24 h. The content was determined according to the weight of residual CNTs.

2.3. Electrochemical Measurements

Electrochemical measurements were conducted in 2032-type coin cells, which were assembled in a high-purity argon-filled glove box. The amorphous Sb₂S₃/CNT nanocomposites were mixed with acetylene black, and carboxy methyl cellulose (CMC) with a ratio of 7:2:1 in deionized water to form slurry. The slurry was pasted on a Cu foil and dried at 80 °C under vacuum for 12 h. The loading density of the electrode laminates was about 1.5 mg cm⁻². Sodium and potassium foils were used as counter and

reference electrodes, respectively. The electrolyte solution was 1 M NaClO₄ and 0.8 M KPF₆ dissolved in ethylene carbonate and diethyl carbonate (1:1 by weight) for NIBs and KIBs, respectively. The separator was the Celgard 2400 membrane. Galvanostatic discharge-charge tests were performed by an Arbin battery testing system (BT-2000). The capacities of the amorphous Sb₂S₃/CNT anode were determined on the basis of the total mass of Sb₂S₃ and CNTs. Electrochemical impedance spectroscopy (EIS) and cyclic voltammetry (CV) measurements were carried out on a Solartron electrochemical workstation.

3. Results and Discussion

3.1. Materials Structure and Morphology

The detailed structural and morphological characterizations of the Sb₂S₃/CNT nanocomposites are shown in Figures 1 and 2. As shown in Figure 1, no obvious sharp diffraction peaks are observed in the XRD pattern of pure Sb₂S₃, indicating the amorphous structure of as-prepared Sb₂S₃. For the Sb₂S₃/CNT nanocomposites, the XRD pattern overlaps well with that of pure Sb₂S₃, except a slightly sharp peak at $2\theta = 26^\circ$ arising from the strongest peak of the CNTs. The results imply that Sb₂S₃ in the nanocomposites is amorphous, and the presence of the CNTs cannot affect the amorphous structure of Sb₂S₃. As can be seen from Figure 2a,b, the amorphous Sb₂S₃ nanospheres grow uniformly on the CNTs. The amorphous Sb₂S₃/CNT nanocomposites interlink and interweave to form a 3D porous conductive network. The amorphous Sb₂S₃/CNT nanocomposites have a diameter range of 30–150 nm, which results from the recombination of pure Sb₂S₃ nanospheres and the CNTs. The grain size of pure Sb₂S₃ micro/nanospheres is in a range of 50–1200 nm, as displayed in Figure S1. The presence of the CNTs inhibits the growth of Sb₂S₃ without changing the spherical morphology. TEM and HRTEM were performed to investigate the microstructure of the CNTs and amorphous Sb₂S₃/CNT nanocomposites. From TEM image (Figure S2a), the CNTs show a wire structure and interconnect to one another. The diameters are in range of 20–90 nm. HRTEM image (Figure S2b) reveals the amorphous carbon microstructure of the CNTs that are composed of short-range ordered nano-crystallites. TEM images (Figure 2c,d) further reveal that the Sb₂S₃ nanospheres with an average particle size of 80 nm are well grown on the CNTs. From the illustration in Figure 2d, the diffuse rings in the selected-area electron diffraction (SEAD) pattern confirm the amorphous structure of Sb₂S₃. Furthermore, the EDX spectrum in Figure 2e undoubtedly proves the nanocomposites contain element Sb, S and C. As expected, the atomic ratio of S and Sb is 1.53. The signals of Cu and O peaks originate from the carbon-coated copper grid. Additionally, the CNTs content is about 21 wt.%, which was determined by using the acid dissolution method.

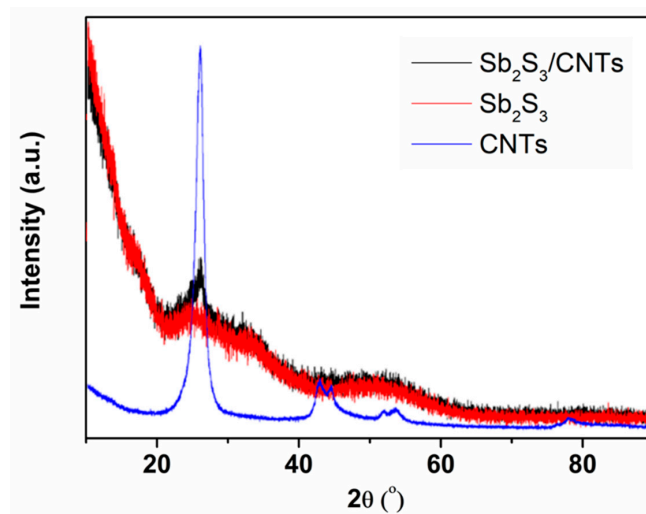


Figure 1. XRD patterns of the as-prepared Sb₂S₃/carbon nanotube (CNT) nanocomposites, pure Sb₂S₃ and CNTs.

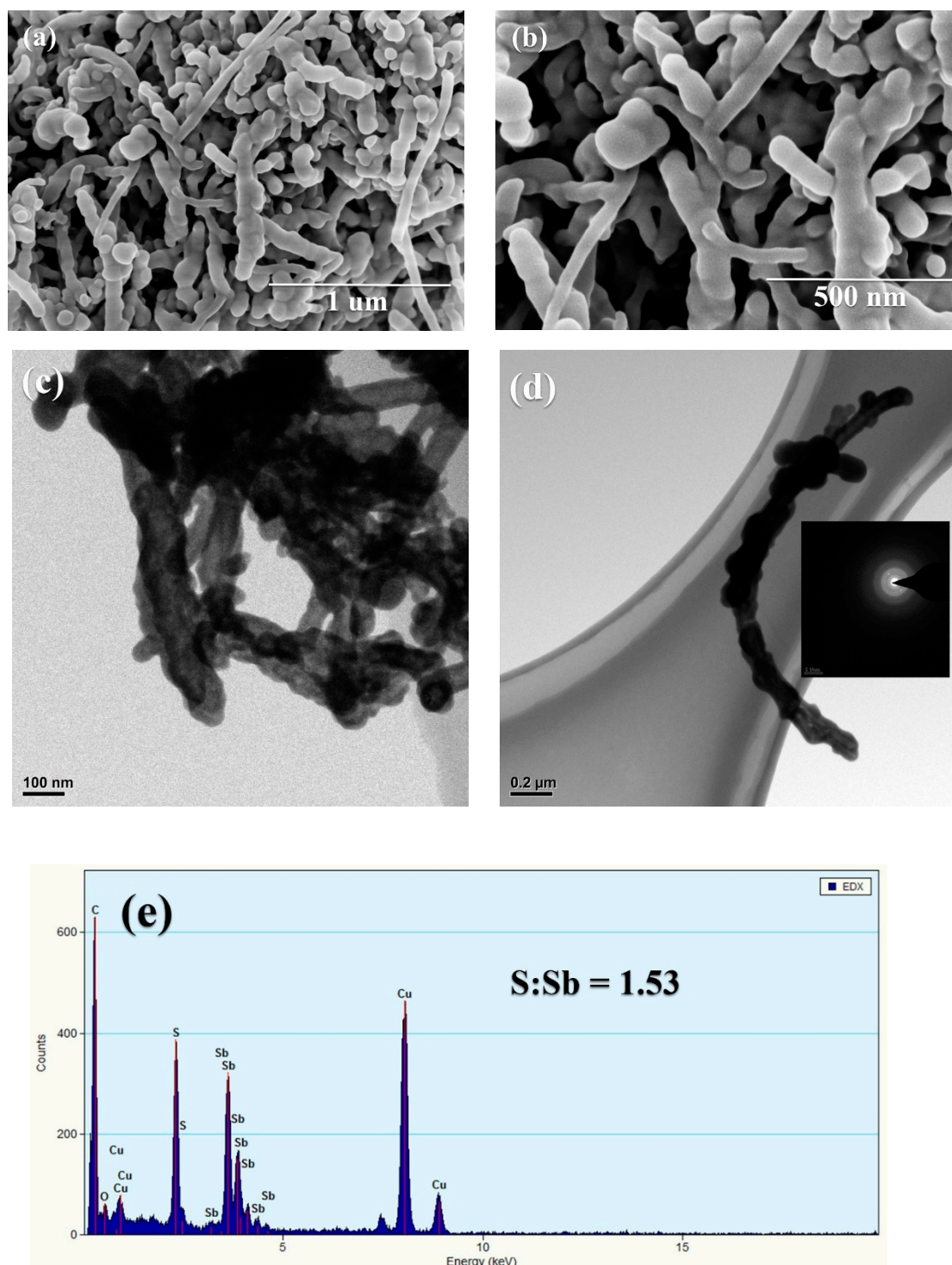


Figure 2. SEM and TEM images of the as-synthesized $\text{Sb}_2\text{S}_3/\text{CNT}$ nanocomposites. (a,b) SEM images, (c,d) TEM images and (e) EDX spectrum. Selected-area electron diffraction (SAED) pattern is illustrated in (d).

3.2. Amorphous $\text{Sb}_2\text{S}_3/\text{CNT}$ Nanocomposites as an Anode for NIBs

Figure 3a displays the CV curves of the amorphous $\text{Sb}_2\text{S}_3/\text{CNT}$ nanocomposites as an anode for NIBs during the initial five cycles at a scan rate of 0.05 mV s^{-1} between 0.01 and 1.5 V (versus Na/Na^+). The first cathodic scan displays two strong current peaks located at 0.83 and 0.41 V, respectively, corresponding to the conversion reaction and alloying reaction of Sb to Na_3Sb (Equations (1) and (2)) [15].

Two oxidation peaks located at 0.8 and 1.3 V in the first anodic scan are assigned to the dealloying and reconversion reactions [26]. A pair of small redox peaks near 0.01 V in the CV curves is assigned to the Na-ion insertion/extraction reaction in the conductive carbon materials (acetylene black) and the CNTs [25]. The subsequent CV curves are almost overlapping, especially the pair of redox peaks of alloying/dealloying reaction, indicating an excellent cycle stability of the $\text{Sb}_2\text{S}_3/\text{CNT}$ anodes.



The discharge/charge plateau regions can be clearly observed in the discharge-charge profiles of the $\text{Sb}_2\text{S}_3/\text{CNT}$ anode under the current density of 100 mA g^{-1} between 0.01 and 1.5 V (Figure 3b), in accordance with the CV curves. The capacities of the $\text{Sb}_2\text{S}_3/\text{CNT}$ anode were calculated on the basis of the total mass of Sb_2S_3 and CNTs. The $\text{Sb}_2\text{S}_3/\text{CNT}$ anode delivers a high initial, reversible charge capacity of 870 mA h g^{-1} and a coulomb efficiency of 77.8%. The initial discharge capacity of 1130 mA h g^{-1} is higher than the theoretical capacity (946 mA h g^{-1}), which can be mainly ascribed to the formation of solid electrolyte interface (SEI) film and the decomposition of the electrolyte. From the Figure 3c, the $\text{Sb}_2\text{S}_3/\text{CNT}$ anode exhibits superior cycling performance at 100 mA g^{-1} , delivering a charge capacity of 704 mA h g^{-1} after 50 cycles, corresponds to 81% of the initial charge capacity. The cycling performance is much higher than that of pure Sb_2S_3 with a reversible capacity of 262 mA h g^{-1} over 25 cycles (Figure S3a).

The rate capability of the $\text{Sb}_2\text{S}_3/\text{CNT}$ anode at various current densities was further studied, as show in Figure 3d and Figure S3b. The discharge capacities of 1280, 831, 795, 743, 685, 601 and 474 mA h g^{-1} can be achieved by cycling at various current densities of 50, 100, 200, 500, 1000, 2000 and 3000 mA g^{-1} . The corresponding charge capacities are 874, 813, 749, 725, 633, 576 and 441 mA h g^{-1} . After 35 discharge-charge cycles, the $\text{Sb}_2\text{S}_3/\text{CNT}$ anode can maintain a discharge capacity of 791 mA h g^{-1} when the current density returns to 50 mA g^{-1} , indicating excellent rate performance. To highlight the superior electrochemical properties of the $\text{Sb}_2\text{S}_3/\text{CNT}$ anode, a comparison of the electrochemical performance of the amorphous $\text{Sb}_2\text{S}_3/\text{CNT}$ nanocomposites with that of previously reported Sb_2S_3 -based anode materials for NIBs is shown in Table 1. As can be seen, the $\text{Sb}_2\text{S}_3/\text{CNT}$ anode is comparable with the reported $\text{Sb}_2\text{S}_3@\text{PPy}$ [21], MWNTs@ $\text{Sb}_2\text{S}_3@\text{PPy}$ [25], $\text{Sb}_2\text{S}_3/\text{graphene}$ [29], hollow-sphere (HS) $\text{Sb}_2\text{S}_3/\text{C}$ [30], $\text{Sb}_2\text{S}_3/\text{PPy}$ [31], sulfur and nitrogen dual doped reduced graphene oxide/ Sb_2S_3 (SN-rGO/ Sb_2S_3) [32], stibnite/sulfur-doped carbon sheet ($\text{Sb}_2\text{S}_3/\text{SCS}$) [33], hierarchical Sb_2S_3 hollow microspheres (Sb_2S_3 HMS) [34] and RGO/ Sb_2S_3 nanorods [35] in terms of initial coulomb efficiency, reversible specific capacity and rate performance. That is attributed to the synergic effects of the amorphous Sb_2S_3 nanospheres and the incorporation of the CNTs. The intrinsic isotropic nature of the amorphous Sb_2S_3 can accommodate the volume change and keep the electrical contact during discharge/charge cycling, particularly in the first cycling, thus facilitating the high initial coulomb efficiency and capacity [19,26]. No obvious morphology differences of the pristine and cycled amorphous Sb_2S_3 -graphite electrodes have been observed by using SEM [26], confirming the structural stability of amorphous Sb_2S_3 during cycling. The amorphous Sb_2S_3 nanospheres can provide more active sites and shorten the diffusion pathway of sodium ion during sodiation/desodiation process, being beneficial to the high capacity and superior rate performance. The 3D porous conductive network composed of the CNTs can well buffer the volume change of Sb_2S_3 and maintain the structural integrity of the electrode [22,25], consequently, leading to a considerable electrochemical performance.

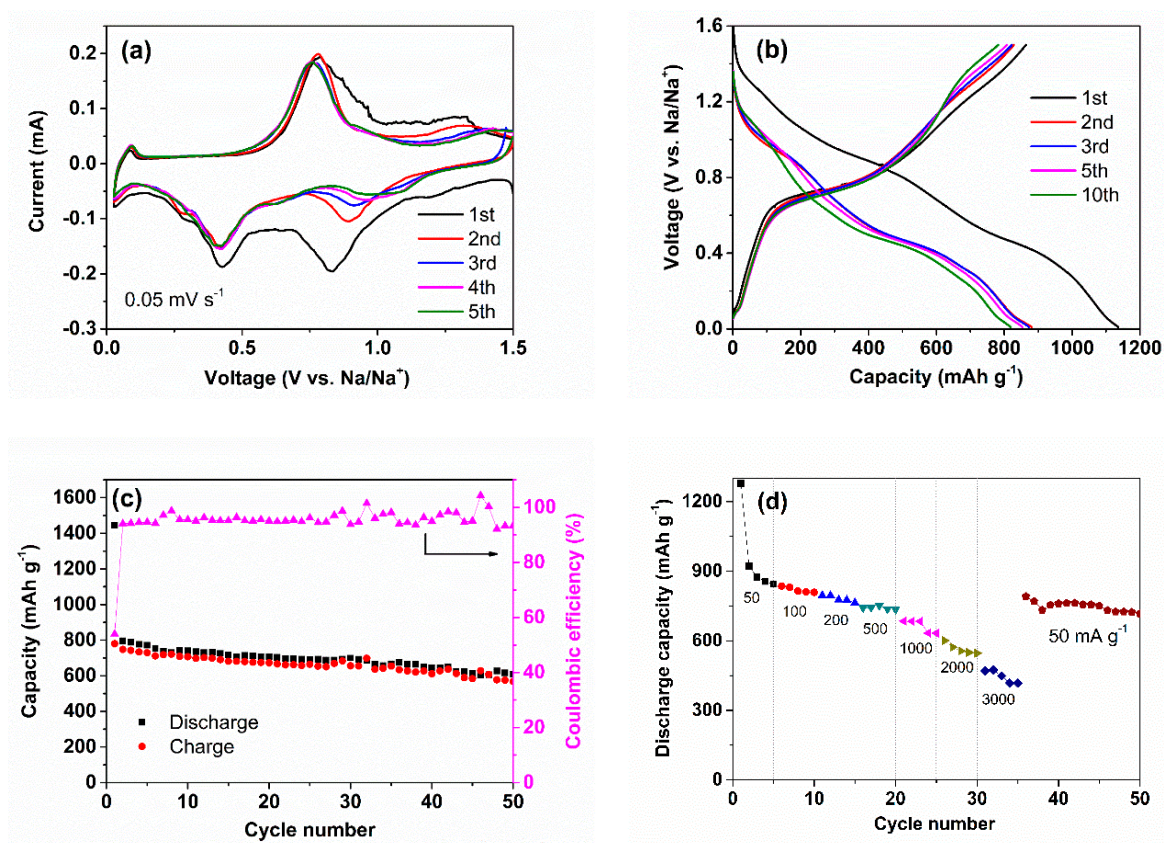


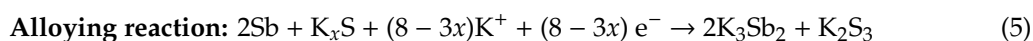
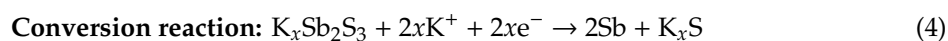
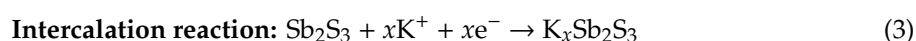
Figure 3. Electrochemical properties of the $\text{Sb}_2\text{S}_3/\text{CNT}$ anode for Na-ion batteries (NIBs) in a voltage range of 0.01–1.5 V. (a) Cyclic voltammetry (CV) curves, (b) galvanostatic discharge-charge profiles measured under a current density of 100 mA g^{-1} , (c) cycling performance at 100 mA g^{-1} and (d) rate capability.

Table 1. Comparison of the electrochemical performance of the amorphous $\text{Sb}_2\text{S}_3/\text{CNT}$ nanocomposites in this work, and those previously reported for Sb_2S_3 -based anode materials for NIBs.

Anode Materials	Initial Coulomb Efficiency	Current Density (mA g^{-1})	Charge Capacity (mAh g^{-1})	Rate Capability ($\text{mAh g}^{-1}/\text{mA g}^{-1}$)	Voltage Cange (V)
Amorphous Sb_2S_3 [19]	65%	50	647	534/3000	0.01–2.5
$\text{Sb}_2\text{S}_3@PPy$ [21]	63.7%	100	860	290/2000	0.01–3.0
MWNTs@ $\text{Sb}_2\text{S}_3@PPy$ [25]	75%	50	626	376/2000	0–2.0
Sb_2S_3 -graphite [26]	84%	100	733	631/3000	0.01–3.0
$\text{Sb}_2\text{S}_3/\text{graphene}$ [29]	65%	50	660	240/1500	0.01–2.0
HS $\text{Sb}_2\text{S}_3/\text{C}$ [30]	64.8%	200	693	220/3200	0.01–3.0
$\text{Sb}_2\text{S}_3/PPy$ [31]	70%	100	605	236/800	0.01–2.5
SN-rGO/ Sb_2S_3 [32]	57%	100	592	365/2000	0.01–2.0
$\text{Sb}_2\text{S}_3/\text{SCS}$ [33]	68.8%	100	642.8	263/1000	0.01–2.5
Sb_2S_3 HMS [34]	62%	200	616	314/3000	0.01–2.0
RGO/ Sb_2S_3 nanorods [35]	52.6%	100	673	381/2000	0.01–2.0
$\text{Sb}_2\text{S}_3/\text{C}$ [36]	78%	50	642	520/2000	0.005–2.0
Multi-shell Sb_2S_3 [37]	55%	100	901	604/2000	0.01–2.0
Amorphous $\text{Sb}_2\text{S}_3/\text{CNT}$ (this work)	77.8%	100	870	441/3000	0.01–1.5

3.3. Amorphous Sb_2S_3/CNT Nanocomposites as an Anode for KIBs

Inspired by the excellent electrochemical characteristics of the amorphous Sb_2S_3/CNT nanocomposites as an anode of NIBs, we further studied their electrochemical performance in KIBs. The potassiation–depotassiation behavior of the Sb_2S_3/CNT anode was firstly investigated by CV technique at a scan rate of 0.05 mV s^{-1} in a range of 0.01 to 3.0 V (versus K/K^+), as shown in Figure 4a. The first CV curve reveals three obvious redox peaks located at 1.35–2.20 V, 0.80–1.37 V and 0.35–1.0 V, which are ascribed to the conversion and alloying reactions during potassiation–depotassiation process [21,23,24]. A small cathodic peak at 1.78 V may be related to the SEI film formation and the intercalation of K-ion into the Sb_2S_3 layered structure. For the subsequent scans, the intensity and location of redox peaks gradually alter, which is due to the structural change of Sb_2S_3 caused by the K-ion insertion/extraction. The reversible potassiation–depotassiation reactions of the Sb_2S_3/CNT anode can be described as in Equations 3–5, which has been confirmed by Lu et al. [23] and Liu et al. [24].



The galvanostatic discharge/charge curves of the Sb_2S_3/CNT anode measured at various current densities in a range of 0.01–2.5V are shown in the Figure 4b. For the first discharge-charge curves at 25 mA g^{-1} , two pairs of obvious discharge/charge plateaus at about 1.1–1.3 V and at 0.5–0.6 V can be observed in the curves, in accordance with the CV curves. In addition, discharge sloping regions from 0.4 to 0.01 V presents in the discharge curve. The results indicate the multistep potassiation–depotassiation processes, including the intercalation reaction, the conversion reaction and alloying reaction. The discharge and charge capacities are 869 and 451 mA h g^{-1} , respectively. The corresponding coulomb efficiency is 52%. The capacity loss is mainly caused by the SEI formation and irreversible side reaction [23]. The charge capacity of the Sb_2S_3/CNT anode is higher than that of the developed anode materials, such as SnS_2-rGO (355 mA h g^{-1} at 25 mA g^{-1}) [16], hard carbon microspheres (262 mA h g^{-1} at 28 mA g^{-1}) [38], Sn–C composite (140 mA h g^{-1} at 25 mA g^{-1}) [39], and MoS_2 (65.4 mA h g^{-1} at 20 mA g^{-1}) [40]. The Sb_2S_3/CNT anode delivers the charge capacities of 446.8, 254.7, 222.2 and 166.6 mA h g^{-1} at different current densities of 50, 100, 500 and 1000 mA g^{-1} (Figure 4c). The cycling performance of the Sb_2S_3/CNT anode at 500 mA g^{-1} is shown in Figure 4d. The first discharge and charge capacities are 691 and 286.5 mA h g^{-1} , respectively, corresponding to an initial coulomb efficiency of 41.5%. After 50 cycles, the reversible capacity is 212.4 mA h g^{-1} , corresponding to a capacity retention of 74.2%. Except the first cycle, the coulomb efficiency is above 95% during the whole cycling. The inferior electrochemical performance of the amorphous Sb_2S_3/CNT nanocomposites in KIBs compared to that in NIBs could be attributed to the large volume expansion, severe pulverization and aggregation, and slower diffusion kinetics of K-ions during the repeated potassiation–depotassiation processes, resulting from the larger ionic radius of the K-ion (1.38 \AA) [21,41]. Similar results have also been reported in VS_2 nanosheet [42] and ReS_2 nanosheets [43]. Additionally, compared to that of the previously reported Sb_2S_3 -based anodes for KIBs (Table 2), the performance of amorphous Sb_2S_3/CNT nanocomposites in this work is poor, indicating the Sb_2S_3/CNT could not deliver their capacities sufficiently during the cycling. The direct growth of Sb_2S_3 nanospheres on the CNTs cannot effectively buffer the volume expansion/contraction and release the mechanical stress of Sb_2S_3 , leading to irreversible potassiation–depotassiation reactions. Those issues can be resolved by surface coating effective conducting agents, or by fabricating nanocomposites with unique morphologies, such as nanosheets, nanotubes and hollow nanospheres.

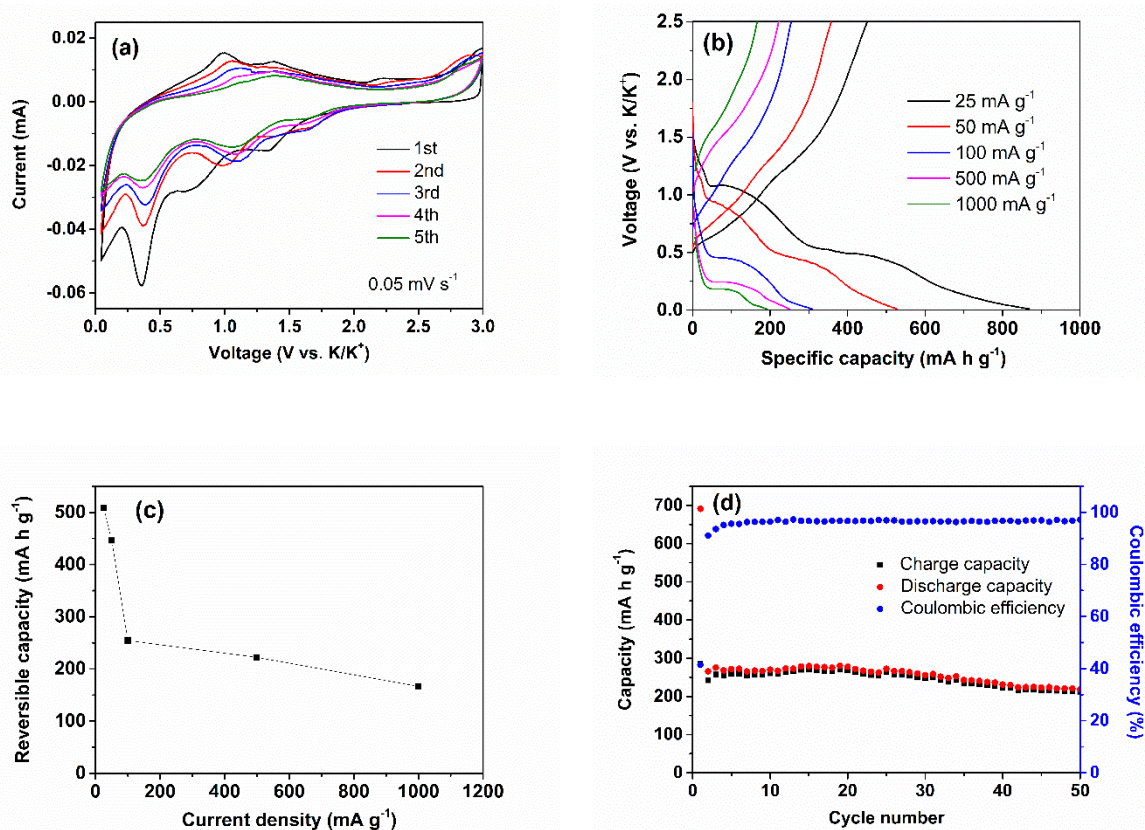


Figure 4. Electrochemical performance of the $\text{Sb}_2\text{S}_3/\text{CNT}$ anode for K-ion batteries (KIBs). (a) CV curves, (b) the galvanostatic discharge-charge curves at various current densities, (c) rate capability and (d) cycling performance at 500 mA g^{-1} .

Table 2. Comparison of the electrochemical performances of the amorphous $\text{Sb}_2\text{S}_3/\text{CNT}$ nanocomposites in this work, and those previously reported for Sb_2S_3 -based anodes for KIBs.

Anode Materials	Charge Capacity ($\text{mA h g}^{-1}/\text{mA g}^{-1}$)	Cycling Performance ($\text{mA h g}^{-1}/\text{n}$)	Rate Capability ($\text{mA h g}^{-1}/\text{mA g}^{-1}$)	Voltage Range (V)	Ref.
$\text{Sb}_2\text{S}_3/\text{PPy}$ coaxial nanorods	628/100	487/18	690/100 280/1000	0.01–3.0	[21]
Sb_2S_3 -SNG composite	537/100	480/100	548/25 340/1000	0.1–3.0	[23]
Amorphous $\text{Sb}_2\text{S}_3/\text{CNT}$	286.5/500	212.4/50	451/25 166.6/1000	0.01–2.5	this work

4. Conclusions

In summary, the amorphous $\text{Sb}_2\text{S}_3/\text{CNT}$ nanocomposites are successfully prepared via in-situ growth of the amorphous Sb_2S_3 nanospheres on the CNTs, constructing a unique nanostructure. The amorphous $\text{Sb}_2\text{S}_3/\text{CNT}$ nanocomposites as an anode for NIBs demonstrate an attractive reversible charge capacity of 870 mA h g^{-1} and a high initial coulomb efficiency of 77.8% at 100 mA g^{-1} . The stable charge capacity is maintained at 704 mA h g^{-1} over 50 cycles. Even at a high current density of 3000 mA g^{-1} , a charge capacity of 474 mA h g^{-1} can be achieved. As an anode for KIBs, the amorphous $\text{Sb}_2\text{S}_3/\text{CNT}$ nanocomposites also demonstrate a high charge capacity of 451 mA h g^{-1} at 25 mA g^{-1} , exceeding the capacities of hard carbon, Sn–C composite and SnS_2 -rGO; but future studies are required to optimize the rate performance and cycling stability. The remarkable performance of the amorphous $\text{Sb}_2\text{S}_3/\text{CNT}$ nanocomposites in NIBs is attributed to the synergic effects of the amorphous Sb_2S_3 nanospheres and 3D porous conductive network composed of the CNTs.

Supplementary Materials: The following are available online at <http://www.mdpi.com/2079-4991/9/9/1323/s1>, Figure S1: SEM image of pure Sb_2S_3 , Figure S2: (a) TEM and (b) HRTEM images of the CNTs, Figure S3: (a) Cycle performance of the Sb_2S_3 anode for NIBs at 100 mA g^{-1} . (b) Galvanostatic discharge-charge profiles of the $\text{Sb}_2\text{S}_3/\text{CNT}$ anode for NIBs measured under various current densities, Figure S4: The galvanostatic discharge/charge curves of the $\text{Sb}_2\text{S}_3/\text{CNT}$ anode for KIBs at 500 mA g^{-1} .

Author Contributions: J.D. and J.P. generated the research idea. M.L., F.H. and J.P. performed the experiments and wrote the original draft. Y.Z. and L.L. participated in the discussions. J.D. and Q.Y. analyzed the data. J.D. and H.Z. polished the manuscript. All authors read and approved the final manuscript.

Funding: This work was funded by the National Natural Science Foundation of China (number 51661009) and the Natural Science Foundation of Guangxi Province (2016GXNSFGA380001). The authors would like to thank the financial support from the key project of Guangxi Key Laboratory of Information Materials (project number 171006-Z).

Conflicts of Interest: The authors declare no conflicts of interest.

References

1. Deng, J.; Luo, W.-B.; Chou, S.-L.; Liu, H.-K.; Dou, S.-X. Sodium-Ion Batteries: From Academic Research to Practical Commercialization. *Adv. Energy Mater.* **2018**, *8*, 1701428. [[CrossRef](#)]
2. Wu, X.; Leonard, D.P.; Ji, X. Emerging Non-Aqueous Potassium-Ion Batteries: Challenges and Opportunities. *Chem. Mater.* **2017**, *29*, 5031–5042. [[CrossRef](#)]
3. Hwang, J.-Y.; Myung, S.-T.; Sun, Y.-K. Sodium-ion batteries: Present and future. *Chem. Soc. Rev.* **2017**, *46*, 3529–3614. [[CrossRef](#)] [[PubMed](#)]
4. Hosaka, T.; Shimamura, T.; Kubota, K.; Komaba, S. Polyanionic Compounds for Potassium-Ion Batteries. *Chem. Rec.* **2019**, *19*, 735–745. [[CrossRef](#)] [[PubMed](#)]
5. Deng, J.; Luo, W.-B.; Lu, X.; Yao, Q.; Wang, Z.; Liu, H.-K.; Zhou, H.; Dou, S.-X. High Energy Density Sodium-Ion Battery with Industrially Feasible and Air-Stable O3-Type Layered Oxide Cathode. *Adv. Energy Mater.* **2018**, *8*, 1701610. [[CrossRef](#)]
6. Wang, X.; Xu, X.; Niu, C.; Meng, J.; Huang, M.; Liu, X.; Liu, Z.; Mai, L. Earth Abundant Fe/Mn-Based Layered Oxide Interconnected Nanowires for Advanced K-Ion Full Batteries. *Nano Lett.* **2017**, *17*, 544–550. [[CrossRef](#)] [[PubMed](#)]
7. Duan, W.; Zhu, Z.; Li, H.; Hu, Z.; Zhang, K.; Cheng, F.; Chen, J. $\text{Na}_3\text{V}_2(\text{PO}_4)_3@C$ core-shell nanocomposites for rechargeable sodium-ion batteries. *J. Mater. Chem. A* **2014**, *2*, 8668–8675. [[CrossRef](#)]
8. Lin, X.; Huang, J.; Tan, H.; Huang, J.; Zhang, B. $\text{K}_3\text{V}_2(\text{PO}_4)_2\text{F}_3$ as a robust cathode for potassium-ion batteries. *Energy Storage Mater.* **2019**, *16*, 97–101. [[CrossRef](#)]
9. Lee, H.-W.; Wang, R.Y.; Pasta, M.; Woo Lee, S.; Liu, N.; Cui, Y. Manganese hexacyanomanganate open framework as a high-capacity positive electrode material for sodium-ion batteries. *Nat. Commun.* **2014**, *5*, 5280. [[CrossRef](#)]
10. Pei, Y.; Mu, C.; Li, H.; Li, F.; Chen, J. Low-Cost $\text{K}_4\text{Fe}(\text{CN})_6$ as a High-Voltage Cathode for Potassium-Ion Batteries. *ChemSusChem* **2018**, *11*, 1285–1289. [[CrossRef](#)]
11. Liu, P.; Li, Y.; Hu, Y.-S.; Li, H.; Chen, L.; Huang, X. A waste biomass derived hard carbon as a high-performance anode material for sodium-ion batteries. *J. Mater. Chem. A* **2016**, *4*, 13046–13052. [[CrossRef](#)]
12. Jian, Z.; Luo, W.; Ji, X. Carbon Electrodes for K-Ion Batteries. *J. Am. Chem. Soc.* **2015**, *137*, 11566–11569. [[CrossRef](#)] [[PubMed](#)]
13. Liu, J.; Wen, Y.; van Aken, P.A.; Maier, J.; Yu, Y. Facile Synthesis of Highly Porous Ni–Sn Intermetallic Microcages with Excellent Electrochemical Performance for Lithium and Sodium Storage. *Nano Lett.* **2014**, *14*, 6387–6392. [[CrossRef](#)] [[PubMed](#)]
14. Wang, Q.; Zhao, X.; Ni, C.; Tian, H.; Li, J.; Zhang, Z.; Mao, S.X.; Wang, J.; Xu, Y. Reaction and Capacity-Fading Mechanisms of Tin Nanoparticles in Potassium-Ion Batteries. *J. Phys. Chem. C* **2017**, *121*, 12652–12657. [[CrossRef](#)]
15. Yu, D.Y.W.; Prikhodchenko, P.V.; Mason, C.W.; Batabyal, S.K.; Gun, J.; Sladkevich, S.; Medvedev, A.G.; Lev, O. High-capacity antimony sulphide nanoparticle-decorated graphene composite as anode for sodium-ion batteries. *Nat. Commun.* **2013**, *4*, 2922. [[CrossRef](#)] [[PubMed](#)]

16. Lakshmi, V.; Chen, Y.; Mikhaylov, A.A.; Medvedev, A.G.; Sultana, I.; Rahman, M.M.; Lev, O.; Prikhodchenko, P.V.; Glushenkov, A.M. Nanocrystalline SnS₂ coated onto reduced graphene oxide: Demonstrating the feasibility of a non-graphitic anode with sulfide chemistry for potassium-ion batteries. *Chem. Commun.* **2017**, *53*, 8272–8275. [[CrossRef](#)]
17. Li, W.; Chou, S.-L.; Wang, J.-Z.; Kim, J.H.; Liu, H.-K.; Dou, S.-X. Sn_{4+x}P₃@Amorphous Sn-P Composites as Anodes for Sodium-Ion Batteries with Low Cost, High Capacity, Long Life, and Superior Rate Capability. *Adv. Mater.* **2014**, *26*, 4037–4042. [[CrossRef](#)]
18. Zhang, W.; Mao, J.; Li, S.; Chen, Z.; Guo, Z. Phosphorus-Based Alloy Materials for Advanced Potassium-Ion Battery Anode. *J. Am. Chem. Soc.* **2017**, *139*, 3316–3319. [[CrossRef](#)]
19. Hwang, S.M.; Kim, J.; Kim, Y.; Kim, Y. Na-ion storage performance of amorphous Sb₂S₃ nanoparticles: Anode for Na-ion batteries and seawater flow batteries. *J. Mater. Chem. A* **2016**, *4*, 17946–17951. [[CrossRef](#)]
20. Hou, H.; Jing, M.; Huang, Z.; Yang, Y.; Zhang, Y.; Chen, J.; Wu, Z.; Ji, X. One-Dimensional Rod-Like Sb₂S₃-Based Anode for High-Performance Sodium-Ion Batteries. *ACS Appl. Mater. Interfaces* **2015**, *7*, 19362–19369. [[CrossRef](#)]
21. Shi, Y.; Li, F.; Zhang, Y.; He, L.; Ai, Q.; Luo, W. Sb₂S₃@PPy Coaxial Nanorods: A Versatile and Robust Host Material for Reversible Storage of Alkali Metal Ions. *Nanomaterials* **2019**, *9*, 560. [[CrossRef](#)] [[PubMed](#)]
22. Li, J.; Yan, D.; Zhang, X.; Hou, S.; Li, D.; Lu, T.; Yao, Y.; Pan, L. In situ growth of Sb₂S₃ on multiwalled carbon nanotubes as high-performance anode materials for sodium-ion batteries. *Electrochimica Acta* **2017**, *228*, 436–446. [[CrossRef](#)]
23. Lu, Y.; Chen, J. Robust self-supported anode by integrating Sb₂S₃ nanoparticles with S,N-codoped graphene to enhance K-storage performance. *Sci. China Chem.* **2017**, *60*, 1533–1539. [[CrossRef](#)]
24. Liu, Y.; Tai, Z.; Zhang, J.; Pang, W.K.; Zhang, Q.; Feng, H.; Konstantinov, K.; Guo, Z.; Liu, H.K. Boosting potassium-ion batteries by few-layered composite anodes prepared via solution-triggered one-step shear exfoliation. *Nat. Commun.* **2018**, *9*, 3645. [[CrossRef](#)] [[PubMed](#)]
25. Wang, S.; Yuan, S.; Yin, Y.-B.; Zhu, Y.-H.; Zhang, X.-B.; Yan, J.-M. Green and Facile Fabrication of MWNTs@Sb₂S₃@PPy Coaxial Nanocables for High-Performance Na-Ion Batteries. *Part. Part. Syst. Charact.* **2016**, *33*, 493–499. [[CrossRef](#)]
26. Zhao, Y.; Manthiram, A. Amorphous Sb₂S₃ embedded in graphite: A high-rate, long-life anode material for sodium-ion batteries. *Chem. Commun.* **2015**, *51*, 13205–13208. [[CrossRef](#)]
27. Xiong, X.; Wang, G.; Lin, Y.; Wang, Y.; Ou, X.; Zheng, F.; Yang, C.; Wang, J.-H.; Liu, M. Enhancing Sodium Ion Battery Performance by Strongly Binding Nanostructured Sb₂S₃ on Sulfur-Doped Graphene Sheets. *ACS Nano* **2016**, *10*, 10953–10959. [[CrossRef](#)] [[PubMed](#)]
28. Yang, H.; Li, M.; Fu, L.; Tang, A.; Mann, S. Controlled Assembly of Sb₂S₃ Nanoparticles on Silica/Polymer Nanotubes: Insights into the Nature of Hybrid Interfaces. *Sci. Rep.* **2013**, *3*, 1336. [[CrossRef](#)]
29. Li, C.-Y.; Patra, J.; Yang, C.-H.; Tseng, C.-M.; Majumder, S.B.; Dong, Q.-F.; Chang, J.-K. Electrolyte Optimization for Enhancing Electrochemical Performance of Antimony Sulfide/Graphene Anodes for Sodium-Ion Batteries—Carbonate-Based and Ionic Liquid Electrolytes. *ACS Sustain. Chem. Eng.* **2017**, *5*, 8269–8276. [[CrossRef](#)]
30. Ge, P.; Hou, H.; Ji, X.; Huang, Z.; Li, S.; Huang, L. Enhanced stability of sodium storage exhibited by carbon coated Sb₂S₃ hollow spheres. *Mater. Chem. Phys.* **2018**, *203*, 185–192. [[CrossRef](#)]
31. Zheng, T.; Li, G.; Zhao, L.; Shen, Y. Flowerlike Sb₂S₃/PPy Microspheres Used as Anode Material for High-Performance Sodium-Ion Batteries. *Eur. J. Inorg. Chem.* **2018**, *2018*, 1224–1228. [[CrossRef](#)]
32. Bag, S.; Roy, A.; Mitra, S. Sulfur, Nitrogen Dual Doped Reduced Graphene Oxide Supported Two-Dimensional Sb₂S₃ Nanostructures for the Anode Material of Sodium-Ion Battery. *ChemistrySelect* **2019**, *4*, 6679–6686. [[CrossRef](#)]
33. Deng, M.; Li, S.; Hong, W.; Jiang, Y.; Xu, W.; Shuai, H.; Li, H.; Wang, W.; Hou, H.; Ji, X. Natural stibnite ore (Sb₂S₃) embedded in sulfur-doped carbon sheets: Enhanced electrochemical properties as anode for sodium ions storage. *RSC Adv.* **2019**, *9*, 15210–15216. [[CrossRef](#)]
34. Xie, J.; Liu, L.; Xia, J.; Zhang, Y.; Li, M.; Ouyang, Y.; Nie, S.; Wang, X. Template-Free Synthesis of Sb₂S₃ Hollow Microspheres as Anode Materials for Lithium-Ion and Sodium-Ion Batteries. *Nano-Micro Lett.* **2017**, *10*, 12. [[CrossRef](#)] [[PubMed](#)]
35. Wen, S.; Zhao, J.; Zhao, Y.; Xu, T.; Xu, J. Reduced graphene oxide (RGO) decorated Sb₂S₃ nanorods as anode material for sodium-ion batteries. *Chem. Phys. Lett.* **2019**, *716*, 171–176. [[CrossRef](#)]

36. Choi, J.-H.; Ha, C.-W.; Choi, H.-Y.; Shin, H.-C.; Lee, S.-M. High performance Sb_2S_3 /carbon composite with tailored artificial interface as an anode material for sodium ion batteries. *Met. Mater. Int.* **2017**, *23*, 1241–1249. [[CrossRef](#)]
37. Xie, F.; Zhang, L.; Gu, Q.; Chao, D.; Jaroniec, M.; Qiao, S.-Z. Multi-shell hollow structured Sb_2S_3 for sodium-ion batteries with enhanced energy density. *Nano Energy* **2019**, *60*, 591–599. [[CrossRef](#)]
38. Jian, Z.; Xing, Z.; Bommier, C.; Li, Z.; Ji, X. Hard Carbon Microspheres: Potassium-Ion Anode Versus Sodium-Ion Anode. *Adv. Energy Mater.* **2016**, *6*, 1501874. [[CrossRef](#)]
39. Sultana, I.; Ramireddy, T.; Rahman, M.M.; Chen, Y.; Glushenkov, A.M. Tin-based composite anodes for potassium-ion batteries. *Chem. Commun.* **2016**, *52*, 9279–9282. [[CrossRef](#)]
40. Ren, X.; Zhao, Q.; McCulloch, W.D.; Wu, Y. MoS_2 as a long-life host material for potassium ion intercalation. *Nano Res.* **2017**, *10*, 1313–1321. [[CrossRef](#)]
41. Li, D.; Sun, Q.; Zhang, Y.; Chen, L.; Wang, Z.; Liang, Z.; Si, P.; Ci, L. Surface-Confined $SnS_2@C@rGO$ as High-Performance Anode Materials for Sodium- and Potassium-Ion Batteries. *ChemSusChem* **2019**, *12*, 2689–2700. [[CrossRef](#)] [[PubMed](#)]
42. Zhou, J.; Wang, L.; Yang, M.; Wu, J.; Chen, F.; Huang, W.; Han, N.; Ye, H.; Zhao, F.; Li, Y.; et al. Hierarchical $VERSUS_2$ Nanosheet Assemblies: A Universal Host Material for the Reversible Storage of Alkali Metal Ions. *Adv. Mater.* **2017**, *29*, 1702061. [[CrossRef](#)] [[PubMed](#)]
43. Mao, M.; Cui, C.; Wu, M.; Zhang, M.; Gao, T.; Fan, X.; Chen, J.; Wang, T.; Ma, J.; Wang, C. Flexible ReS_2 nanosheets/N-doped carbon nanofibers-based paper as a universal anode for alkali (Li, Na, K) ion battery. *Nano Energy* **2018**, *45*, 346–352. [[CrossRef](#)]



© 2019 by the authors. Licensee MDPI, Basel, Switzerland. This article is an open access article distributed under the terms and conditions of the Creative Commons Attribution (CC BY) license (<http://creativecommons.org/licenses/by/4.0/>).